DOI: 10.1002/chem.200902435

Evolution of Helical Mesostructures

Pei Yuan,[a, b] Lingzhi Zhao,[a] Nian Liu,[a] Guangfeng Wei,[a] Yunhua Wang,[a] Graeme J. Auchterlonie,[c] J. Drennan,[c] Gao Qing Lu,[d] Jin Zou,*[b, c] and Chengzhong Yu*[a, d]

Abstract: An intriguing evolution from a simple internal helix to a hierarchical helical (HH) mesostructure with both internal and external helices or a complicated screwlike and concentric circular (CC) mesostructure is successfully observed. The complicated helical structures are determined by TEM studies and 3D electron tomography. We demonstrate a topological helix–coil transition between the internal and external helices to reveal the origin of the HH mesostructure and the relationship between the straight helical and HH rods. Moreover, the boundary condition of the helix–coil transition is clarified to explain in detail the formation of complex helical structures, such as the screwlike mesostructure. It is proposed that the final structural characteristics are determined exactly by the balance between the decrease in the surface free energy and the maintenance of the hexagonal packing in one individual rod, which explains the formation of unusual CC, HH, and screwlike morphologies in one pot. Our success has opened new opportunities in the characterization of complex porous architectures, thus paving a way to remarkable advances in the fields of synthesis, understanding, and application of novel porous materials.

Keywords: electron tomography · helical structures · helix–coil transition · self-assembly · surfactants

Introduction

Novel porous materials have attracted extensive attention over past decades as a result of their scientific importance and applications in many technological fields.[1–5] With recent progressive developments, helical mesoporous materials with both traditional crystallographic symmetry elements and unconventional helical symmetry have become a globally focused topic because of their potential applications in chiral synthesis, chiral separation, chiral catalysis, and chiral recognition.[6–8] Che et al.[9] were the first to report the synthesis of chiral mesoporous materials by using chiral surfactants as templates. Since then, numerous helical mesostructures have been successfully prepared in the presence of either chiral or achiral surfactants, such as the straight helical structure with only an internal helix (twist),[10–13] a hierarchal helical (HH) structure with both internal and external (spiral) helices,[13–15] a double helix (two single helices winding together),[16] a triplet helix (one helix winds around a double helix),[16] and so forth.

The HH mesostructure is one of the most intriguing but complicated architectures that is constructed by further spiraling the twisted hexagonal straight rod into a second-level helical morphology with both internal and external helices. It is noted that in the case of complicated helical mesostructures, the mesostructure itself is generally limited to hexagonal symmetry, whereas the internal and external helical symmetries are independent, thus may have a large variety of tunable parameters. It is expected that the integration of the rich helical structural elements together with the hexagonal

[a] P. Yuan, L. Zhao, N. Liu, G. Wei, Prof. Y. Wang, Prof. C. Yu
Department of Chemistry and Shanghai Key Laboratory of Molecular Catalysis and Innovative Materials
Fudan University, 220 Handan Road
Shanghai, 200433 (China)
Fax: (+86) 21-6564-1740
E-mail: czyu@fudan.edu.cn

[b] P. Yuan, Prof. J. Zou
Division of Materials
The University of Queensland
Brisbane, QLD 4072 (Australia)
E-mail: j.zou@uq.edu.au

[c] G. J. Auchterlonie, Prof. J. Drennan, Prof. J. Zou
Centre for Microscopy and Microanalysis
The University of Queensland
Brisbane, QLD 4072 (Australia)

[d] Prof. G. Q. Lu, Prof. C. Yu
ARC Centre of Excellence for Functional Nanomaterials
The University of Queensland
Brisbane, QLD 4072 (Australia)

Supporting information for this article is available on the WWW under http://dx.doi.org/10.1002/chem.200902435.

mesostructure may result in a number of novel and fascinating architectures, including different HH mesostructures and even more complicated helical mesostructures. Comprehensive analysis of these helical mesostructures is of vital importance in understanding their formation mechanism and future applications.

Up to now, various complicated helical mesostructures have been reported;[9–17] however, the detailed structural information and the origin of their unique morphologies have not been demonstrated.[9,10,13,15] Importantly, the relationship between the well-studied straight internal helical structure and the complicated HH mesostructures has not been reported until now. On one hand, there have been few methods to simply synthesize a series of helical mesostructures with different helical parameters. On the other hand, it is rather difficult to characterize the detailed structure of each complicated helix by using bulk techniques such as N_2 physisorption, XRD, or conventional TEM, then to explore the structural transformation among different complicated helical mesostructures.

Herein, a variety of helical mesostructured materials have been successfully synthesized by using an achiral surfactant (octadecyltrimethylammonium bromide (C_{18}TAB)) as a template and perfluorooctanoic acid (PFOA) as an additive through a base-catalyzed silica sol–gel process. With increasing weight ratios ϕ of PFOA/C_{18}TAB from 0 to 0.1, an evolution from a straight internal helical to HH mesostructure with both internal and external helices or screwlike[16,17] and concentric circular (CC)[18–23] mesostructures is observed. The recently developed 3D TEM technique, that is, electron tomography (ET),[23–27] was carried out to successfully determine the complex screwlike helical architectures. More importantly, we demonstrate a topological helix–coil transition model to successfully explain the structural evolution of different helical mesostructures. Although the helix–coil transition model has been applied in polypeptides to measure the molecule in an α-helix conformation versus a turn or random coil,[28–31] it is applied herein to a much more complicated mesostructure with not only two helical operations but also a 2D hexagonal packing symmetry. The boundary condition of the helix–coil transition is also clarified to explain in detail the formation of complex helical structures, such as the screwlike mesostructure. It is proposed that the final complex structural characteristics are determined by the balance between the decrease in the surface free energy and the maintenance of the hexagonal packing in each individual rod. Our studies provide new opportunities in the characterization of complex porous architectures, thus shedding light on the synthesis, understanding, and application of novel porous materials.

Results

General characterization of the helix mesostructure: Samples **S0–S3** were characterized by XRD and N_2 physisorption (see Figures S1 and S2, respectively, in the Supporting Information). The physicochemical parameters of **S0–S3** are listed in Table 1 for comparison. The small-angle XRD patterns display three diffraction peaks in the range $2\theta = 2$–$5°$ for the calcined samples **S0–S2** (Figure S1 in the Supporting Information), which can be indexed as the 10, 11, and 20 reflections based on a 2D hexagonal symmetry (*p6m*).[32] When the ϕ value of PFOA/C_{18}TAB is increased, the width of the diffraction peaks are broadened, thus leading to less-resolved diffraction peaks. For **S3**, the ordering of the mesostructure disappears as observed by the broad diffraction peak with low intensity. Samples **S0–S3** exhibit type-IV isotherms with type *H1* hysteresis loops in N_2 adsorption/desorption isotherms (Figure S2a in the Supporting Information). The steep capillary condensation step occurs at the same position ($P/P_0 = 0.30$–0.45) and the mean pore size is 2.9 nm in all four samples (Figure S2b in the Supporting Information). Again, the width of the mesopore-size distribution curve is broadened with an increasing ϕ value of PFOA/C_{18}TAB. It is noted that a second capillary condensation step occurs at $P/P_0 > 0.9$ in the adsorption isotherm of **S3**, which is indicative of textural interparticle porosity.

Table 1. Physicochemical properties of mesoporous materials **S0–S3** prepared at different weight ratios ϕ of PFOA/C_{18}TAB.

Sample	ϕ	d [nm][a]	p [nm][b]	S [$m^2 g^{-1}$][c]	V [$cm^3 g^{-1}$][d]
S0	0:1	4.0	2.9	748	0.71
S1	0.025:1	4.0	2.9	767	0.99
S2	0.05:1	4.0	2.9	650	0.99
S3	0.10:1	3.8	2.7	593	1.54

[a] Calculation of the d spacing from the first XRD peak. [b] Pore size was calculated from the adsorption branch by using the Barrett-Joyner-Halenda (BJH) method. [c] BET surface area. [d] Pore volume.

SEM images show that **S0** (synthesized in the absence of PFOA) has a near spherical morphology (approximately 100 nm in diameter; Figure S3a in the Supporting Information). For **S1**, SEM imaging reveals an approximately 100% rodlike morphology with a length of approximately 300 nm and diameters between 60 and 100 nm (Figure S3b in the Supporting Information). For **S2**, rodlike and some spherical-like morphologies could be obtained (Figure S3c in the Supporting Information). The rodlike morphology almost vanishes in **S3**, and only aggregated nanosized particles are observed (Figure S3d in the Supporting Information).

TEM observations reveal that most of the **S0** particles are indeed not spheres as observed by SEM (Figure S3a in the Supporting Information), but have a short cylindrical-like morphology (Figure 1a). Relative to **S1**, which has a rodlike morphology (Figure 1c,d), the difference with **S0** is that the aspect ratio (the length of the rod versus its diameter) of the **S1** rods is much larger than that of the **S0** rods. From the side view of the **S0** rods (Figure 1a), a clear fringe (indicated by black arrows) that corresponds to the (10) plane of a helical hexagonal mesostructure is observed for most of the rods.[13] The twisting pitch P_t cannot be calculated because the helical **S0** rods are too short to observe two adja-

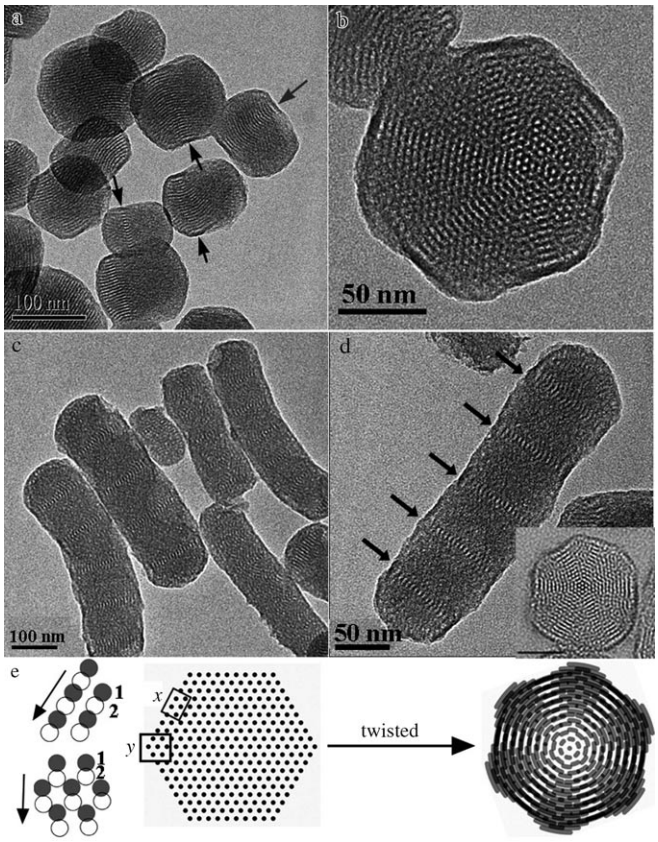

Figure 1. TEM images of a,b) **S0** and c,d) **S1**. a) Side and b) top views of internal helical short rods. The black arrows in (a) and (d) indicate the fringes of the helices. The inset of (d) is the cross section of **S1** prepared with the ultramicrotome (thin section: ~50 nm) and the scale bar is 50 nm. e) Simulated model to illustrate the ✱-type pattern observed in Figure 1b. Gray circles (1) in (e) indicate the original pore positions before twisting and white circles (2) indicate the subsequent pore positions after twisting. The black arrows in (e) indicate the direction of the displacement along the <10> and <11> planes in regions *x* and *y*, respectively.

cent (10) fringes. Nevertheless, it can be estimated that the P_t value is definitely larger than 600 nm in **S0**. From the top view of an **S0** particle (Figure 1b), a hexagonal shape with a honeycomb arrangement of bright dots (pore channels) is observed, thus indicating that the hexagonally ordered 1D channels are parallel to the long axis of the rod.

High-yield helical mesostructured rods 60–80 nm in width and 250–300 nm in length can be obtained in **S1** (Figure 1c). From a high-magnification image (Figure 1d), the recurrent fringes (indicated by dark arrows) are clearly visible along the length of the helical rods and correspond to the (10) planes. The cross-sectional TEM image of **S1**, prepared with the ultramicrotome, also shows the dotlike pores in a hexagonal array at the centre (inset of Figure 1d). The twisting pitch, which is six times the distance between two adjacent (10) fringes, is calculated to be approximately 450 nm (Figure 1d). TEM observations have shown that both **S0** and **S1** are conventional internal helical structures as reported previously.[9–15]

Cross-section of the ✱-type pattern in the helix mesostructure: It is interesting to note an unusual ✱-type pattern composed of six fringes can be observed in Figure 1b. Each fringe starts from the centre and extends to the midpoint of the six edges of the hexagon. The origin of this unusual pattern can be illustrated by the schematic model shown in Figure 1e. When viewed from the long axes of the rods (the [001] direction), ordered hexagonal packing dots should be observed before twisting, each black dot represents one straight pore channel in a calcined sample or a threadlike micelle in an as-synthesized sample. However, when the rod is slightly twisted, the projection of the helical (originally straight) pore channels will generate a trace of displacement along the view direction. The length of such a displacement is dependent on the helical parameters and the thickness of the TEM specimen, which should be constant for a given specimen composed of pore channels of equal length. The direction of the displacement, on the other hand, is influenced by the hexagonal geometry. To make this point clear, two representative regions *x* and *y* are magnified in Figure 1e (left), which are located near the midpoint and vertex of one side of the hexagon, respectively. The black arrows indicate the directions of displacements (i.e., the tangent direction of twisting), which is along the <10> and <11> plane in regions *x* and *y*, respectively (Figure 1e).

The above analysis can also be applied equally to the silica wall (instead of the pore channels) because either the pore channels or the silica walls can be regarded as elements that have hexagonal symmetry. Principally, the TEM image reveals the mass-thickness depth information, thus the displacement of pore channels induced by the helical conformation, however, cannot be observed. What can be observed in the TEM images is indeed the projection of the helical silica walls. Therefore, when the displacement occurs only in the (10) plane any adjacent two (10) planes can still be observed in region *x* of Figure 1e. Nevertheless, the pore channel right in the middle of the rod is straight in the helical mesostructured rods, and the curvature of a helical pore channel increases as the distance between the channel and the centre of the rod enlarges. As a result, the length of the displacement for one helical pore channel along the long axes of the rods also increases with increasing distance from the centre of the rod. Thus, relative to the structure before twisting, the only difference is the occurrence of continuous line patterns of the silica walls, whereas the hexagonally arrayed dotlike pore channels cannot be observed after twisting. This phenomenon is more enhanced for the (10) planes away from the centre of the rod, but not distinctive near the centre in which the hexagonally arrayed bright dots (pore channels) can still be observed.

When the displacement occurs in region *y* of Figure 1e, such displacements will "insert" into two adjacent (11) planes in which the pores should be located. Thus, the black-and-white contrast between the wall and pore becomes blurred in this region. The 3D simulated model after twisting is shown in Figure 1e (right), which is in good agreement with our experimental observation of the ✱-type

pattern (Figure 1b). It should be noted that a similar phenomenon can be also observed in the cross-sectional image of **S1** (inset of Figure 1d), thus confirming that the ✱-type pattern is an intrinsic structural reflection of internal helical mesostructures.

Complicated helical mesostructure from a one-pot synthesis: When the ϕ value of PFOA/C_{18}TAB is increased to 0.05:1, various complicated helical structures are obtained simultaneously. Their representative TEM images are shown in Figure 2, including HH structures (Figure 2a–c), the screwlike structure (Figure 2d), the CC structure (Figure 2e), and the coiled structure (Figure 2f). Similar HH mesostructured rods shown in Figure 2a–c have variable helical structural parameters (Table 2). The HH rods shown in Figure 2a,b have relatively larger external pitch sizes (ca. 279 and 165 nm) and diameters (ca. 83 and 74 nm, respectively), whereas the HH rod in Figure 2c has a smaller external pitch size of approximately 76 nm and a diameter of approximately 49 nm. It is consistent with the well-documented facts that the pitch of the internal helical mesostructures decreases when the rod diameter is decreased.[10,33–35]

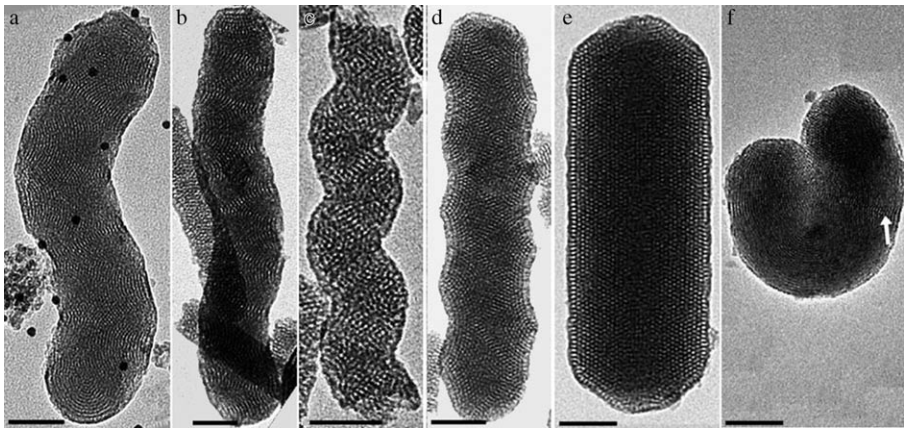

Figure 2. TEM images of the typical helical morphologies found in **S2**. a–c) HH structures with internal and external helical mesostructures, d) screwlike mesostructures, e) CC structure, and f) coiled structure. The white arrow in (f) indicates the internal helical fringe. The scale bar is 50 nm.

An interesting and apparently more complicated screwlike mesostructure with wavelike edges can also be observed in the one-pot synthesis at PFOA/C_{18}TAB $\phi = 0.05$ (Figure 2d). The screwlike structures can be easily found under TEM observations (Figure S4 in the Supporting Information). To understand the detailed complicated pore architecture, ET was performed on a typical screwlike rod given in Figure 3a. The tomographic slices selected from the top, middle, and bottom in the x–y plane along the z axis are displayed in Figure 3b–d, respectively. From the top and bottom slices, it is interesting to note that the external helical direction (indicated by black lines) is almost parallel to the pore channels, thus indicating that the screwlike structure has a close external helix without an internal helix, which definitely has a different organization relative to the HH rods. (For comparison, the ET slice images of screwlike and HH rods are shown in Figure S5 in the Supporting Information.) In addition, it can be directly seen from the tomographic 3D reconstruction shown in Figure 3e that this screwlike rod has a close external helix with an external pitch size P_s of 85 nm, as determined by measuring the distance between two convex points (see Figure S6 in the Supporting Information for the detailed measurement).

Table 2. Helical parameters of the HH rods shown in Figure 2a–c.

Sample	P_s [nm][a]	R [nm][b]	r [nm][c]	κ[d]	$1/\kappa$ [nm][e]
Figure 2a	279.0	21.4	41.4	0.0088	113.5
Figure 2b	164.7	9.6	36.8	0.0123	81.2
Figure 2c	76.0	8.1	24.5	0.0382	26.2

[a] External helical pitch of the HH rods. [b] Radius of the external helix. [c] Radius of the helical rod. [d] Bending curvature. [e] Radius of the external helical curvature.

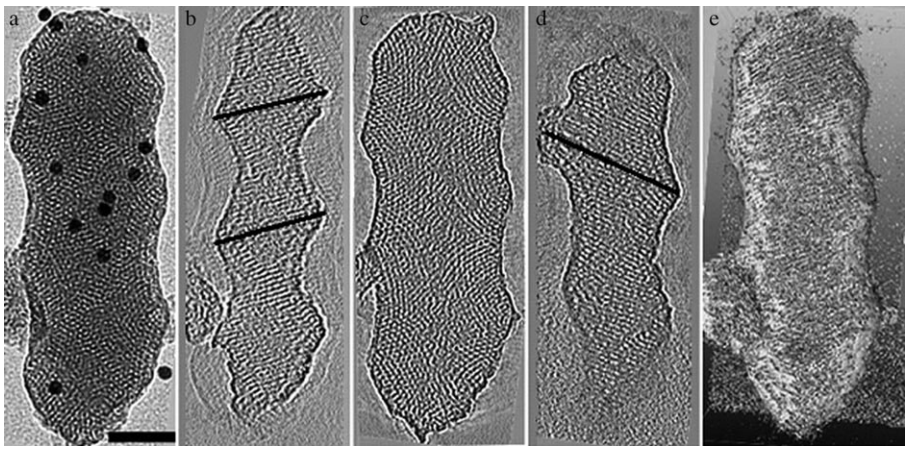

Figure 3. The TEM image of a) a typical screwlike rod and b–d) ET slices along the z axis at the top, middle, and bottom positions. Black lines indicate the direction of the external helix which is parallel to pore channels. e) Three-dimensional reconstruction of the screwlike rod. The scale bar is 50 nm.

Some helical mesostructures with coiled shapes can also be obtained at PFOA/C_{18}TAB $\phi=0.05$ (Figure 2e), which shows only one visible (10) fringe as indicated by the white arrow. This coiled structure can be topologically transformed from an internal helical structure (twisted rod), which is quite similar with the prevalent helix–coil transition model in polypeptides,[28–31] but much more complicated due to the hexagonal mesostructural symmetry and two helical operations (internal and external). This issue will be discussed later.

When the ϕ value of PFOA/C_{18}TAB is further increased to 0.1:1, the typical TEM image of **S3** shows disordered mesostructures interwoven with some multilamellar vesicles (Figure S6 in the Supporting Information). The phase transformation from the ordered hexagonal mesostructure to multilamellar vesicles as the ϕ value of PFOA/C_{18}TAB increases has been observed before in a PFOA/cetyltrimethylammonium bromide (C_{16}TAB) templating system,[36] also in agreement with the XRD pattern of **S3** (Figure S1 in the Supporting Information), which shows only a broad diffraction peak with low intensity.

Discussion

Topological helix–coil transition of internal and external helices: In the base-catalyzed PFOA/C_{18}TAB system, the origin of the internal helical conformation can be attributed to the decrease in surface free energy during the transformation process from a nonhelical rod (composed of hexagonally arrayed straight threadlike composite micelles of equal length) to a twisted helical mesostructure.[10] The agent PFOA, with a very low surface tension, plays an important role in the interfacial interaction to induce the formation of helical mesostructures with decreased pitch sizes. In an internal helical hexagonal mesostructure, the curvature of each threadlike micelle (note: the removal of micelles creates the pore channels) is dependent on its location and increases with increasing distance from the center of the rod.[10,13] Theoretically, the assembly of threadlike micelles with different curvatures cannot form an ideal hexagonal organization and may break the hexagonal symmetry to a certain degree. When the pitch size of an internal helical structure is decreased, the curvature of the threadlike micelle at a given location increases, which leads to further derivation from a perfect hexagonal symmetry. Relative to **S0** and **S1**, **S2** synthesized at a higher ϕ value of PFOA/C_{18}TAB has a smaller diameter, and thus its internal helical structure should have an even smaller pitch size,[10,33–35] thus leading to a much tighter internal helical configuration and less-ordered hexagonal mesostructure. By assuming that the hexagonal symmetry is a stable mesostructure at a given synthetic regime in our synthesis, an optimum structure with both minimized derivation from perfect hexagonal packing (considering the mesostructure assembly) and maximized decrease in the surface free energy (considering the helical morphology) should be compromised. Thus, the transformation between the internal and external helices is important to understand the formation of different complicated helical mesostructures with a range of helical parameters.

In topology, the structure of a twisted rod with one pitch can be equivalently transformed into a coiled rod with bending of 360° without twisting (Figure 4 and Movie 1 in the Supporting Information). For a pure external helical mesostructure without twisting, all the pore channels are parallel to each other and no curvature difference between composite micelles at different locations exists, which allows for perfect hexagonal packing. Therefore, the transformation from an internal helical configuration to an external helical structure favors a closely packed and ordered hexagonal mesostructure. However, for a pure external helical mesostructure, its surface area is the same relative to a straight rod with the same hexagonal mesostructure, thus the decrease in the surface free energy as the driving force to form the internal helical structure is lost. In addition, relative to a straight hexagonal mesostructured rod, the pure external helical mesostructure without twisting has the same mesostructure but an increase in bending energy. As a consequence, it is expected for an internal helical mesostructure with a very small pitch size that the release of the twisting, to a certain extent, is advantageous to form a compromised HH structure.

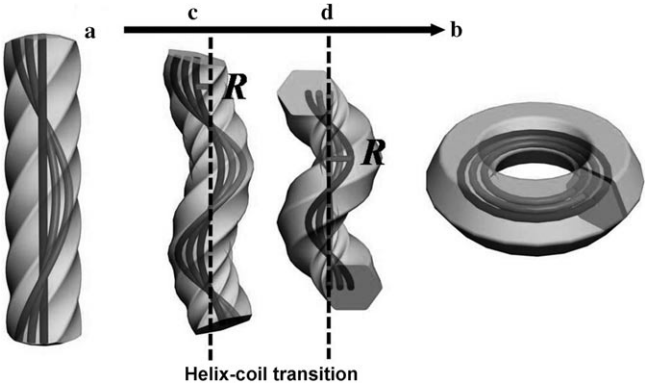

Figure 4. Schematic model that illustrates the helix–coil transition from a twisted internal helical rod with one pitch (a) to a coiled rod with bending of 360° without twisting (b). The helix–coil transition process is simulated in Movie 1 (see the Supporting Information). The hierarchical internal and external helical structures with different spiral radius R and P_s values (c and d) are regarded as the intermediate transition states during this process.

To support our proposed mechanism on the transformation of the internal/external helical configuration in different complicated helical mesostructures, the following calculation was performed to quantitatively describe the helix–coil transition model in HH structures. For simplification, we started with a pure internal helical mesostructured rod (Figure 4a) with one pitch (P_t) and a length of l ($l=P_t$), which can be equivalently transformed to a coiled mesostructure without any twisting (Figure 4b). The helix–coil transition process is simulated in Movie 1 in the Supporting Information. The

HH structures with different R and P_s values (see Figure 4c,d) are, therefore, regarded as the intermediate transition states during this process. It should be noted that the external and internal helices possess the same orientation during the transition process. By assuming that the length of the threadlike micelles is constant, the relationship of the geometrical parameters during the transition process can be described as

$$l = 2\pi\sqrt{R^2 + C^2} \quad (1)$$

Equation (1) can also be used to describe the internal helical mesostructure (Figure 4a, where $R=0$; R is the radius of external helix) and the coiled mesostructure without twisting (Figure 4b, where $P_s=0$, or $C=P_s/2=0$; thus, $l=2R$). The twisting curvature λ and bending curvature κ are introduced to represent the extent of the internal and external helices separately within a HH structure, which are defined by Equations (2) and (3).

$$\lambda = \frac{C}{R^2 + C^2} \quad (2)$$

$$\kappa = \frac{R}{R^2 + C^2} \quad (3)$$

The internal helical angle α and external helical angle γ can be calculated by Equations (4) and (5).

$$\alpha = \lambda l = \frac{2\pi C}{\sqrt{R^2 + C^2}} \quad (4)$$

$$\gamma = \kappa l = \frac{2\pi R}{\sqrt{R^2 + C^2}} \quad (5)$$

For the internal helical mesostructure (Figure 4a), $\alpha=2\pi$ and $\gamma=0$. For the coiled mesostructure without twisting (Figure 4b), $\alpha=0$ and $\gamma=2\pi$. In the cases of the HH structures with internal and external helices (Figure 3c,d), the α and γ values can be calculated by using geometric parameters based on Equations (4) and (5). Moreover, the relationship between the α and γ values can be obtained from Equations (4) and (5) as $\alpha^2+\gamma^2=4\pi^2$, which is a constant. Therefore, α decreases as γ increases, thus indicating that the internal helix can be released with the occurrence of an external helix. It is noted that in the case of an originally straight internal helical rod with a pitch size that is not equal to 2π (e.g., the helical rods shown in Figure 2a–c), the α and γ values can also be calculated (for details see the text in the Supporting Information). For a normalized comparison of helical rods with different pitch sizes, the value of γ/l, that is, κ, can be used to measure the amount of internal helix released. For the experimentally observed helical rods shown in Figure 2a–c, the value of κ is calculated and given in Table 2 with geometric parameters, such as the radius of the rods r, R, and P_s.

It can be seen that the value of κ increases as the value of r decreases (Table 2). As discussed before, an internal helical rod with a smaller r value should have tighter internal twisting,[10,33–35] which is not advantageous to form an ordered hexagonal mesostructure. Because the internal helical-to-coiled structure transition can release the internal twisting to maintain a close-packing hexagonal structure, it is expected that an internal helical mesostructured rod with a smaller r value should release more internal twisting (i.e., larger κ value) through the formation of the external helix. The experimentally observed relationship between κ and r is consistent with our proposed helix–coil transition model. Moreover, the direct observation of the coiled helical rod (see Figure 2e) with only one (10) fringe implies that the internal-to-external helix transformation occurs to a large extent, which also supports our proposed helix–coil transition model. In addition, this model can also be used to explain the experimental observation as to why both the internal and external helices must possess the same orientation.[13]

The boundary condition of the helix–coil transition: Although the helix–coil transition can release the internal helix, such a transition has a topological restriction, which comes from the topological relationship between the radius of the bending curvature ($1/\kappa$) and r. The function $1/\kappa$ is dependent on both the P_s and R variables according to Equation (3), which can be alternatively expressed by Equation (6).

$$\frac{1}{\kappa} = \frac{R^2 + C^2}{R} \quad (6)$$

For a given rod, R^2+C^2 is a constant [Equation (1)] and both R and C values can be determined; thus, the value of $1/\kappa$ is theoretically proportional to the value of $1/R$, which can be represented by the curve shown in Figure 5a. To illustrate the boundary condition of the helix–coil transition, Figure 5b–d illustrates three model spiral rods with the same r value but decreased $1/\kappa$ value as R increases or P_s decreases. It can be clearly seen that to avoid the formation of a collapsed spiral morphology, the criterion of $1/\kappa \geq r$ must be satisfied (Figure 5b,c). A collapsed spiral rod forms

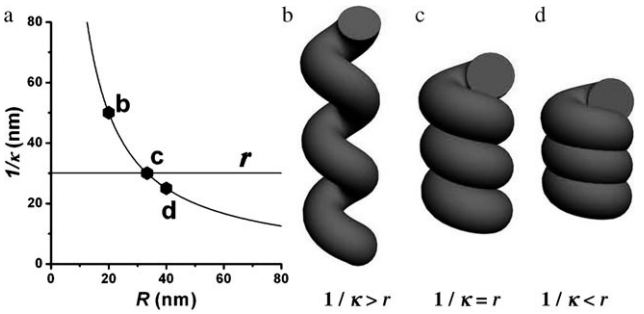

Figure 5. a) Plot of $1/\kappa$ as a function of R ($1/\kappa=(R^2+C^2)/R$, where R is the radius of the external helix and $C=P_s/2\pi$). Schematic models of three different spiral rods in which the helical rods have the same radius r but different radius of external helical curvature ($1/\kappa$): b) $1/\kappa>r$, c) $1/\kappa=r$, and d) $1/\kappa<r$.

when $1/\kappa < r$ (Figure 5d), thus resulting in overlapping and disturbance of two originally hexagonally arrayed domains.

The above discussion is applied to explain the observed different helical mesostructures shown in Figure 2a–d, and their theoretical functions of $1/\kappa$ and R can be determined (see Figure 6a–d for the respective results). For the HH

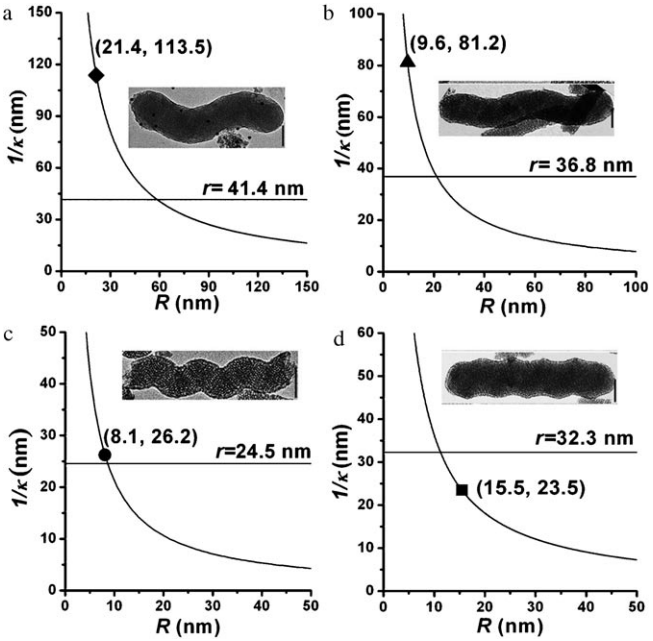

Figure 6. a–d) Relationships of $1/\kappa$ versus r that show the boundary condition of the helix–coil transition of the helical rods in Figure 2a–d (inset is the corresponding TEM image), respectively. The symbols in (a–d) indicate the coordinated positions of each rod and the parameters (R, r, and $1/\kappa$) are measured from the TEM images (Table 2 and Table S1 in the Supporting Information).

rods with relatively larger values of r (i.e., 41.4 and 36.8 nm, insets in Figure 6a,b, respectively), the corresponding values of $1/\kappa$ (i.e., 113.5 and 81.2 nm, respectively) are thus larger. As a consequence, $1/\kappa > r$ is satisfied in both cases (Figure 6a,b), which are far from the topological boundary condition, and in turn the formation of an external spiral morphology has no restriction. When the r value is decreased to 24.5 nm (inset in Figure 6c), the $1/\kappa$ value is decreased to 26.2 nm, which is approaching, but still above, the borderline (Figure 6c). However, for the screwlike complicated helical structure with a quite different morphology (inset of Figure 6d), the r value is difficult to be measured accurately, but is definitely larger than 32.3 nm (for the detailed measurement see Figure S7 in the Supporting Information), and the $1/\kappa$ value is calculated to be approximately 23.5 nm, thus indicating that the screwlike helical structure exists under the borderline topological restriction. It is expected that at least partial merging of the rod and reorganization of mesostructures occurs in the screwlike rod due to the topological restriction. However, the new type of screwlike rod has the same tendency of r to $1/\kappa$ as in the HH rods (Table 2), that is, the $1/\kappa$ value decreases as the r value decreases (see Table S1 in the Supporting Information). The screwlike mesostructure with an external helical morphology is suggested to form with considerable stability due to the decrease in the surface area in the merging and restructuring process.

Evolution of complicated helical mesostructures: The evolution process of the helical mesostructures can be summarily illustrated in Figure 7. As the ϕ value of PFOA/C_{18}TAB increases from 0:1 to 0.05:1, the particles grew from short

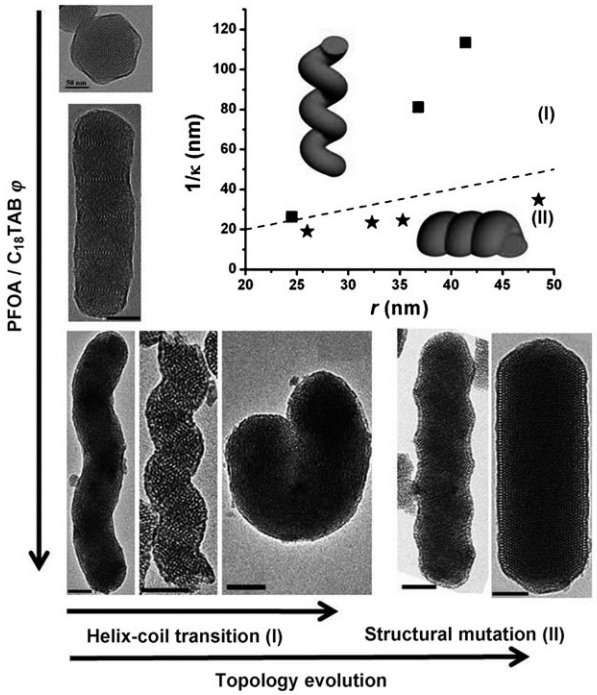

Figure 7. A schematic illustration that demonstrates the evolution of helical mesostructures (shown by TEM images). The graph (upper right) describes the relationship of $1/\kappa$ and r to show topological evolution. The dashed line is the boundary condition of $1/\kappa = r$, above which is the helix–coil transition (region I) and below is region II in which the collapsed spirals are formed and structure mutation occurs. ■ represents HH rods shown in Figure 2a–c and ★ represents the screwlike mesostructures shown in Figure S4 in the Supporting Information. The scale bar is 50 nm.

straight rods with a large internal helical pitch of approximately >600 nm (**S0**) to a longer straight rod with a internal helical pitch of approximately 450 nm (**S1**) then to various complicated helical architectures (**S2**). However, along with this process, a loosely packed and less-ordered hexagonal structure is formed. By taking the minimum derivation from a closely packed hexagonal mesostructure and the maximum decrease in the surface free energy into consideration, a variety of complicated helical architectures in the one-pot synthesis appears as the result of the topological transformation and structural mutation. The HH structure with both internal and external helices is formed during the helix–coil transition process (region I), so that a compromised point can be achieved to efficiently release the close internal helix and

mitigate the breakage of the ordered hexagonal symmetry. The observed relationship between κ and r in which an internal helical mesostructured rod with a smaller r value releases more internal twisting (for a larger κ value see the black squares in Figure 7) is in good agreement with our proposed helix–coil transition model, which also explains the formation of HH structures with a variety distribution of fringes.

Alternatively, the internal–external helical transition has a restriction defined by the boundary condition of $1/\kappa = r$ (the dashed line in Figure 7). Below this topological boundary, the complicated screwlike mesostructure forms (black stars in Figure 7), which can be regarded to be a result of a structural mutation in this restricted region (II). The screwlike structure has only the external helix, thus there is no curvature difference between the micelles, which may be favorable to maintain the ordered hexagonal symmetry. Moreover, the screwlike structure has the largest release of the internal helix and an alternative method to decrease the surface area by partial volume overlapping. However, the structural organization within the screwlike rod at any given region is not known, especially at those places in which volume overlapping occurs. The CC mesostructure, on one hand, can be regarded as an alternative topologically mutated organization of a perfect hexagonal symmetry. On the other hand, the external surface area of the cylindrical rod is about 95% of a hexagonal rod with a constant cross-sectional area,[21] thus implying that all of these unusual mesostructures, that is, the CC, internal helical, HH, and complex screwlike morphologies, may have the same origin, namely, the decrease in the surface free energy.

Conclusions

An evolution from a straight internal helical to HH mesostructure or screwlike and CC mesostructures has been successfully observed by varying the weight ratio of two cotemplates through a base-catalyzed silica sol–gel process. On the basis of the mathematical calculations, a topological helix–coil transition model is proposed to explain this structural evolution and reveal the origin of the HH mesostructure and the transition from the internal to external helical structures. Moreover, the evolution between different helical mesostructures synthesized in a one-pot procedure can be established based on the boundary condition of the helix–coil transition. The balance between the decrease in surface free energy and maintenance of hexagonal packing in each individual rod determines its final complex structural characteristic. Our proposed model may be applied to explain the formation of helical morphologies, which is important in the design and controlled synthesis of new materials.

Experimental Section

All the chemicals were used as received without further purification. C_{18}TAB and PFOA were purchased from Aldrich. The other chemicals were purchased from the Shanghai Chemical Company. The mesostructured materials were synthesized under basic conditions with C_{18}TAB as a template and PFOA as an additive.[10] In a typical synthesis, C_{18}TAB (0.20 g) was dissolved in deionized water (96 g) with stirring at room temperature. NaOH (2 M, 0.70 mL) and a desired amount of PFOA were added separately to the solution. The weight ratio ϕ of PFOA/C_{18}TAB was 0:1, 0.025:1, 0.05:1, and 0.1:1 and the four samples were designated as **S0**, **S1**, **S2**, and **S3**, respectively. The temperature of the solution was raised to and kept at 80 °C. Tetraethyl orthosilicate (TEOS; 1.34 mL) was added to this solution with stirring and the reaction mixture was stirred continuously for 2 h. The precipitates were collected by filtration, washed with deionized water, and dried in air at room temperature. The as-synthesized samples were calcined at 550 °C for 5 h in air to remove the templates.

XRD patterns of the mesostructural materials were recorded on a Bruker D4 Endeavor diffractometer using Ni-filtered $Cu_{K\alpha}$ radiation at a voltage of 40 kV and a working current of 40 mA. TEM investigations were performed in an FEI Tecnai T12 microscope operated at 120 kV. For TEM observation, the specimens were prepared by dispersal of the powders in ethanol and dried onto holey carbon films supported on standard TEM Cu grids. Nitrogen adsorption/desorption isotherms were measured at −196 °C by using a Micromeritics ASAP Tristar 3000 system. Prior to examination, the samples were degassed at 180 °C overnight on a vacuum line. SEM observations were performed on a Philips XL30 microscope operated at 25 kV. The cross-section TEM specimens were prepared with an ultramicrotome (Leica ultracut 63) and the thickness of the section was approximately 50 nm. Electron tomography was performed with an FEI Tecnai F30 transmission electron microscope operating at 300 kV. All the TEM images were digitally recorded at a given defocus in a bright-field mode. Alignment and 3D reconstructions of HH structures by filtered back projection were performed with IMOD and AMIRA software.[36–39]

Acknowledgements

We thank the State Key Research Program (2010CB226901, 2006CB932302), the NSF of China (20721063), Shanghai STC (08DZ2270500, 07QH14003), SLADP (B108, B113), the Ministry of Education of China (20060246010), and the Australian Research Council for their financial support. We thank Dr. Matthias Floetenmeyer from CMM of UQ for help with the fiducial markers and the ultramicrotome experiments.

[1] G. Cavallaro, P. Pierro, F. S. Palumbo, F. Testa, L. Pasqua, R. Aiello, *Drug Delivery* **2004**, *11*, 41–46.
[2] N. K. Mal, M. Fujiwara, Y. Tanaka, *Nature* **2003**, *421*, 350–353.
[3] D. E. De Vos, M. Dams, B. F. Sels, P. A. Jacobs, *Chem. Rev.* **2002**, *102*, 3615–3640.
[4] M. E. Davis, *Nature* **2002**, *417*, 813–821.
[5] T. Linssen, K. Cassiers, P. Cool, E. F. Vansant, *Adv. Colloid Interface Sci.* **2003**, *103*, 121–147.
[6] D. Bradshaw, T. J. Prior, E. J. Cussen, J. B. Claridge, M. J. Rosseinsky, *J. Am. Chem. Soc.* **2004**, *126*, 6106–6114.
[7] X. Yan, F. Wei, S. P. Elangovan, M. Ogura, T. Okubo, *Eur. J. Inorg. Chem.* **2004**, 4547–4549.
[8] H. B. Qiu, Y. Inoue, S. N. Che, *Angew. Chem.* **2009**, *121*, 3115–3118; *Angew. Chem. Int. Ed.* **2009**, *48*, 3069–3072.
[9] S. Che, Z. Liu, T. Ohsuna, K. Sakamoto, O. Terasaki, T. Tatsumi, *Nature* **2004**, *429*, 281–284.

[10] S. Yang, L. Z. Zhao, C. Z. Yu, X. F. Zhou, J. W. Tang, P. Yuan, D. Y. Chen, D. Y. Zhao, *J. Am. Chem. Soc.* **2006**, *128*, 10460–10466.
[11] B. Wang, C. Chi, W. Shan, Y. H. Zhang, N. Ren, W. L. Yang, Y. Tang, *Angew. Chem.* **2006**, *118*, 2142–2144; *Angew. Chem. Int. Ed.* **2006**, *45*, 2088–2090.
[12] H. B. Qiu, S. G. Wang, W. B. Zhang, K. Sakamoto, O. Terasaki, Y. Inoue, S. Che, *J. Phys. Chem. C* **2008**, *112*, 1871–1877.
[13] T. Ohsuna, Z. Liu, S. N. Che, O. Terasaki, *Small* **2005**, *1*, 233–237.
[14] J. G. Wang, W. Q. Wang, P. C. Sun, Z. Y. Yuan, B. H. Li, Q. H. Jin, D. T. Ding, T. H. Chen, *J. Mater. Chem.* **2006**, *16*, 4117–4122.
[15] Y. Han, L. Zhao, J. Y. Ying, *Adv. Mater.* **2007**, *19*, 2454–2459.
[16] G. L. Lin, Y. H. Tsai, H. P. Lin, C. Y. Tang, C. Y. Lin, *Langmuir* **2007**, *23*, 4115–4119.
[17] S. M. Yang, W. J. Kim, *Adv. Mater.* **2001**, *13*, 1191–1195.
[18] F. Kleitz, F. Marlow, G. D. Stucky, F. Schuth, *Chem. Mater.* **2001**, *13*, 3587–3595.
[19] F. Marlow, A. S. G. Khalila, M. Stempniewicz, *J. Mater. Chem.* **2007**, *17*, 2168–2182.
[20] F. Marlow, B. Spliethoff, B. Tesche, D. Y. Zhao, *Adv. Mater.* **2000**, *12*, 961–965.
[21] J. F. Wang, C. K. Tsung, W. B. Hong, Y. Y. Wu, J. Tang, G. D. Stucky, *Chem. Mater.* **2004**, *16*, 5169–5181.
[22] Y. Y. Wu, G. S. Cheng, K. Katsov, S. W. Sides, J. F. Wang, J. Tang, G. H. Fredrickson, M. Moskovits, G. D. Stucky, *Nat. Mater.* **2004**, *3*, 816–822.
[23] P. Yuan, N. Liu, L. Z. Zhao, X. F. Zhou, L. Zhou, G. J. Auchterlonie, X. D. Yao, J. Drennan, G. Q. Lu, J. Zou, C. Z. Yu, *Angew. Chem.* **2008**, *120*, 6772–6775; *Angew. Chem. Int. Ed.* **2008**, *47*, 6670–6673.
[24] I. Arslan, T. J. V. Yates, N. D. Browning, P. A. Midgley, *Science* **2005**, *309*, 2195–2198.
[25] H. Friedrich, J. R. A. Sietsma, P. E. de Jongh, A. J. Verkleij, K. P. de Jong, *J. Am. Chem. Soc.* **2007**, *129*, 10249–10254.
[26] Z. Y. Li, N. P. Young, M. Di Vece, S. Palomba, R. E. Palmer, A. L. Bleloch, B. C. Curley, R. L. Johnston, J. Jiang, J. Yuan, *Nature* **2008**, *451*, 46–48.
[27] P. A. Midgley, E. P. W. Ward, A. B. Hungria, J. M. Thomas, *Chem. Soc. Rev.* **2007**, *36*, 1477–1494.
[28] H. Imamura, M. Kato, *Proteins Struct. Funct. Bioinf.* **2009**, *75*, 911–918.
[29] S. Piana, *J. Phys. Chem. A* **2007**, *111*, 12349–12354.
[30] Z. Reich, S. Levinzaidman, S. B. Gutman, T. Arad, A. Minsky, *Biochemistry* **1994**, *33*, 14177–14184.
[31] F. C. Zegarra, G. N. Peralta, A. M. Coronado, Y. Q. Gao, *Phys. Chem. Chem. Phys.* **2009**, *11*, 4019–4024.
[32] C. T. Kresge, M. E. Leonowicz, W. J. Roth, J. C. Vartuli, J. S. Beck, *Nature* **1992**, *359*, 710–712.
[33] H. Y. Jin, Z. Liu, T. Ohsuna, O. Terasaki, Y. Inoue, K. Sakamoto, T. Nakanishi, K. Ariga, S. N. Che, *Adv. Mater.* **2006**, *18*, 593–596.
[34] H. Y. Jin, H. B. Qiu, C. B. Gao, S. A. Che, *Microporous Mesoporous Mater.* **2008**, *116*, 171–179.
[35] H. B. Qiu, S. N. Che, *J. Phys. Chem. B* **2008**, *112*, 10466–10474.
[36] S. Yang, X. F. Zhou, P. Yuan, M. H. Yu, S. G. Xie, J. Zou, G. Q. Lu, C. Z. Yu, *Angew. Chem.* **2007**, *119*, 8733–8736; *Angew. Chem. Int. Ed.* **2007**, *46*, 8579–8582.
[37] J. R. Kremer, D. N. Mastronarde, J. R. McIntosh, *J. Struct. Biol.* **1996**, *116*, 71–76.
[38] AMIRA homepage: http://www.tgs.com/products/amira.asp.
[39] Further experimental details are given in the Supporting Information.

Received: September 3, 2009
Published online: December 10, 2009

